Research Square

Preprints are preliminary reports that have not undergone peer review.
They should not be considered conclusive, used to inform clinical practice,
or referenced by the media as validated information.

A Lesion-Guided Deep Learning Framework for Differential Diagnosis of Pulmonary Nodules: A Pathology-Confirmed Study of Pulmonary Tuberculosis, Lung Cancer, Pulmonary Cryptococcosis, and Other Granulomatous Lung Lesions

Ying Hu
First Affiliated Hospital Zhejiang University
Chensong Xu
First Affiliated Hospital Zhejiang University
Sijie Qian
First Affiliated Hospital Zhejiang University
Tingwei Xu
First Affiliated Hospital Zhejiang University
Xukun Li
Hangzhou AiSmartVision Co., Ltd
Weibo Du
First Affiliated Hospital Zhejiang University
Wei Wu
1198042@zju.edu.cn

First Affiliated Hospital Zhejiang University

Research Article

Keywords: Lesion-guided, Dual-branch, 3D, Differentiation, Pulmonary nodule, Tuberculosis, Deep learning

Posted Date: November 11th, 2026

DOI: https://doi.org/10.21203/rs.3.rs-11302345/v1

License: This work is licensed under a Creative Commons Attribution 4.0 International License.
Read Full License

Additional Declarations: No competing interests reported.

A Lesion-Guided Deep Learning Framework for Differential Diagnosis of Pulmonary Nodules: A Pathology-Confirmed Study of Pulmonary Tuberculosis, Lung Cancer, Pulmonary Cryptococcosis, and Other Granulomatous Lung Lesions

Ying Hu[a], Chensong Xu[ab], Sijie Qian[a], Tingwei Xu[a], Xukun Li[c], Weibo Du[a], Wei Wu[ad]

a. State Key Laboratory for Diagnosis and Treatment of Infectious Diseases, National Clinical Research Center for Infectious Diseases, Collaborative Innovation Center for Diagnosis and Treatment of Infectious Diseases, the First Affiliated Hospital, School of Medicine, Zhejiang University, Hangzhou, Zhejiang, China.

b. The author contributed equally to this work.

c. Artificial Intelligence Lab, Hangzhou AiSmartVision Co., Ltd., Hangzhou, Zhejiang, China

The correspongding author, Email: 1198042@zju.edu.cn; Phone number:13957142269

Abstract

Background: Pulmonary tuberculous nodules frequently exhibit imaging features that overlap with those of lung cancer, pulmonary cryptococcosis, and other granulomatous lesions, making accurate preoperative diagnosis challenging and often resulting in unnecessary surgical intervention. We developed a lesion-guided deep learning framework to improve the differential diagnosis of surgically resected pulmonary nodules on chest CT.

Methods: This single-center retrospective study included 1,084 patients with surgically confirmed pulmonary nodules, comprising pulmonary tuberculosis (n = 240), pulmonary cryptococcosis (n = 298), other granulomatous inflammatory lesions (n = 252), and lung malignancies (n = 294). We developed a lesion-guided dual-branch UNet (LG-DU-Net) that jointly performed lesion segmentation and classification in an end-to-end framework. Model performance was compared with five representative deep learning models using multiple binary and multi-class classification tasks.

Results: LG-DU-Net consistently achieved the best diagnostic performance across all classification tasks. In benign–malignant classification, the model achieved an AUC of 0.880. The highest performance was observed in differentiating pulmonary tuberculosis from pulmonary cryptococcosis, with an AUC of 0.972 and an accuracy of 89.8%. In the three-class classification task involving pulmonary tuberculosis, pulmonary cryptococcosis, and other granulomatous inflammatory lesions, the model achieved a macro-average AUC of 0.862. Grad-CAM visualization demonstrated that model predictions were primarily driven by lesion-related imaging features.

Conclusion: LG-DU-Net enables accurate and interpretable differentiation of pulmonary tuberculosis, lung cancer, pulmonary cryptococcosis, and other granulomatous pulmonary nodules using chest CT images. The proposed framework has the potential to improve preoperative diagnostic accuracy, facilitate appropriate clinical management, and reduce unnecessary surgical intervention.

Keywords: Lesion-guided; Dual-branch; 3D; Differentiation; Pulmonary nodule; Tuberculosis; Deep learning

1. Introduction

Pulmonary nodules are frequently encountered on chest computed tomography (CT), and accurate preoperative differentiation between benign and malignant lesions is critical for appropriate clinical management[1]. In tuberculosis-endemic regions, pulmonary tuberculous nodules represent one of the most common benign lesions that mimic lung cancer[2-4]. Because pulmonary tuberculosis, pulmonary cryptococcosis, and other granulomatous inflammatory lesions often share overlapping CT features with malignant tumors, distinguishing these entities based solely on imaging remains challenging[5, 6]. Consequently, many patients undergo unnecessary surgical resection before a definitive pathological diagnosis is established[7].

Chest CT plays a central role in the evaluation of pulmonary nodules because of its high spatial resolution and ability to depict lesion morphology, internal attenuation, and relationships with surrounding structures[8-10]. However, considerable overlap exists in the imaging appearances of pulmonary tuberculosis, pulmonary cryptococcosis, granulomatous inflammatory lesions, and early-stage lung cancer. Although certain imaging signs, including satellite lesions, cavitation, calcification, and halo signs, may provide diagnostic clues, their interpretation remains subjective and depends heavily on radiologist experience.

Artificial intelligence has shown considerable promise in chest imaging over the past decade[11-14]. Deep learning models have achieved excellent performance in pulmonary nodule detection, lung cancer screening, and tuberculosis identification on both chest radiographs and CT images[15-17]. Nevertheless, most existing studies have focused on

binary classification, particularly the differentiation of benign and malignant nodules[18] or pulmonary tuberculosis versus lung cancer[2, 19, 20]. Moreover, many models rely on manually delineated regions of interest or handcrafted radiomic features, limiting their reproducibility and clinical applicability.

More importantly, pulmonary cryptococcosis and other granulomatous inflammatory lesions have received relatively little attention in previous deep learning studies despite being frequent causes of benign pulmonary nodules encountered in clinical practice. Differentiating these diseases from pulmonary tuberculosis and lung cancer remains one of the most challenging tasks in thoracic imaging because of their overlapping radiological appearances and distinct therapeutic strategies. Therefore, there remains a need for an automated and interpretable deep learning framework capable of addressing this clinically relevant differential diagnostic scenario.

In this study, we developed a lesion-guided dual-branch deep learning framework (LG-DU-Net) for the differential diagnosis of pulmonary tuberculosis, lung cancer, pulmonary cryptococcosis, and other granulomatous inflammatory lesions on chest CT. Using a large surgically confirmed cohort, we evaluated its performance across multiple clinically relevant binary and multi-class classification tasks and compared it with representative two-dimensional and three-dimensional deep learning models.

2. Materials and Methods

2.1 Study Subjects

This single-center retrospective study was conducted in accordance with the Declaration of Helsinki and was approved by the Ethics Committee of the First Affiliated Hospital, Zhejiang University School of Medicine (Approval No. ZDYHLS2024Y0534-Quick).The requirement for informed consent was waived because only previously archived, de-identified clinical and imaging data were used. Two distinct patient cohorts from the same period and same center were retrospectively screened. The first cohort consisted of 3,430 patients who underwent surgical resection for pulmonary nodules at the First Affiliated Hospital of Zhejiang University School of Medicine between January 2019 and March 2024, with postoperative pathological findings indicative of granulomatous inflammation. The second cohort comprised patients with pathologically confirmed pulmonary malignancies from the same center during the same period.

2.1.1. Pathological Classification

All surgical specimens underwent routine hematoxylin and eosin (H&E) staining for histopathological evaluation. Specimens showing granulomatous inflammation were further examined using Ziehl–Neelsen acid-fast staining, Gomori methenamine silver (GMS) staining, periodic acid–Schiff (PAS) staining, mucicarmine staining, *Mycobacterium tuberculosis* fluorescence in situ hybridization (TB-FISH), and fungal fluorescence in situ hybridization (fungal FISH), as appropriate. The diagnosis of all cases was confirmed by two pathologists through independent review of the slides. Pulmonary tuberculosis was diagnosed based on histopathological evidence of necrotizing granulomatous inflammation with caseous necrosis, supported by positive

Ziehl–Neelsen acid-fast staining and/or positive Mycobacterium tuberculosis fluorescence in situ hybridization (TB-FISH) or polymerase chain reaction (TB-PCR). Pulmonary cryptococcosis was diagnosed by the presence of encapsulated yeast organisms within granulomatous lesions on histopathological examination, confirmed by periodic acid–Schiff (PAS) staining, Gomori methenamine silver (GMS) staining, and/or positive fungal fluorescence in situ hybridization (fungal FISH). For the other pulmonary granulomatous inflammation group, it refers to granulomas in which pulmonary tuberculosis and cryptococcal nodules were excluded through the aforementioned examinations.

2.1.2. Inclusion Criteria:

a) Patients with pulmonary nodules who underwent surgical resection and were histopathologically diagnosed with one of the following conditions: pulmonary tuberculosis, pulmonary cryptococcosis, other granulomatous inflammatory lesions (excluding pulmonary tuberculosis and pulmonary cryptococcosis), or lung malignancy (including, but not limited to, adenocarcinoma, squamous cell carcinoma, and small cell lung cancer).
b) Availability of preoperative thin-section non-contrast chest CT images with one or more clearly identifiable pulmonary nodules.

2.1.3. Exclusion Criteria:

a) Age <18 years.

b) CT images with severe motion artifacts or image noise that precluded accurate lesion delineation or feature extraction.

c) Coexisting pulmonary diseases that could confound pathological diagnosis or imaging interpretation, including concomitant bacterial infection or lung malignancy.

d) Receipt of disease-specific treatment before CT examination or surgical resection, including anti-infective therapy, chemotherapy, or radiotherapy.

2.1.4 Patient Selection and Matching

From the granulomatous inflammation cohort (n = 3,430), cases were initially classified into three groups based on pathological diagnosis: pulmonary tuberculosis (n = 324), pulmonary cryptococcosis (n = 320), and other pulmonary granulomatous inflammation (n = 1,814). After applying the inclusion and exclusion criteria, 240 patients with pulmonary tuberculosis and 298 patients with pulmonary cryptococcosis were deemed eligible. To minimize potential bias arising from differences in demographic characteristics, patients with lung malignancies and other pulmonary granulomatous inflammation were selected using age- and sex-matched sampling based on the pulmonary cryptococcosis cohort (n = 298). This resulted in the inclusion of 294 patients with lung malignancies and 252 patients with other pulmonary granulomatous inflammation from their respective source cohorts. After screening and matching, a total of 1,084 patients were included in the final study cohort, comprising 240 patients with pulmonary tuberculosis, 298 with pulmonary cryptococcosis, 252 with other pulmonary granulomatous inflammation, and 294 with lung malignancies (Figure 1).

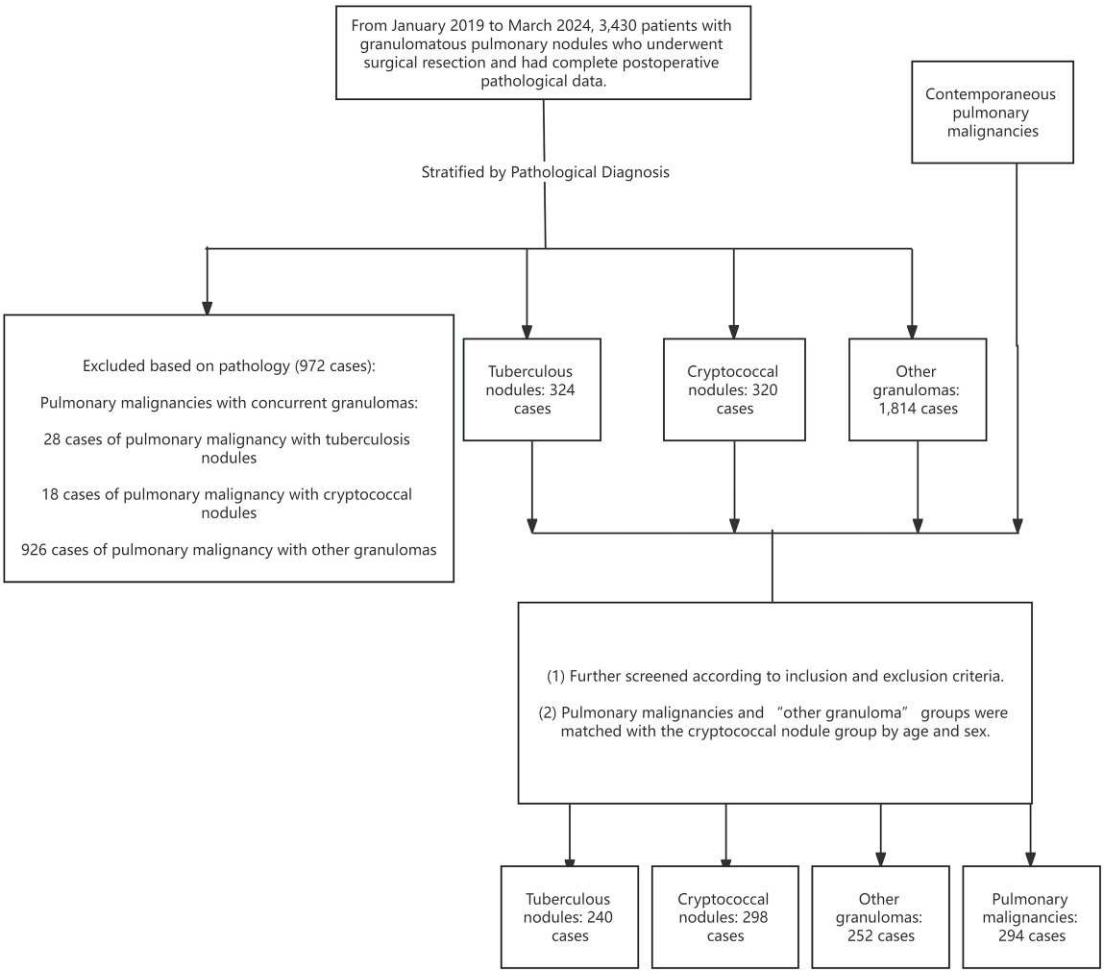


Figure 1 Patient Flowchart

2.1.5 Collection of Clinical Data

Clinical data were retrospectively collected from the hospital electronic medical record system for patients with pulmonary tuberculosis (n = 240). Demographic characteristics, clinical symptoms, underlying comorbidities, laboratory findings (including immunological, microbiological, and tumor marker tests), and imaging features were recorded.

2.1.6 CT Image Acquisition

Chest CT images were retrospectively retrieved from the Picture Archiving and Communication System (PACS) of the First Affiliated Hospital of Zhejiang University School of Medicine. To ensure consistency of model inputs, only preoperative non-contrast CT scans were included. For patients who underwent both non-contrast and contrast-enhanced examinations, only the non-contrast image series acquired before contrast administration were analyzed. All CT images were exported in Digital Imaging and Communications in Medicine (DICOM) format after de-identification and used for model development and evaluation.

2.1.7 CT Lesion Annotation

To generate pixel-level annotations for model training, all **1,084** patients CT scans were independently annotated in three dimensions by two trained researchers using **ITK-SNAP** under the supervision of a thoracic radiologist with more than 10 years of experience. Lesion contours were manually delineated on each CT slice to include the entire lesion, including solid components, calcifications, cavitation, and satellite lesions. Discrepancies between the two annotators were resolved by consensus with the supervising radiologist, and all annotations underwent final quality review. Binary lesion masks (lesion = 1, background = 0) were subsequently generated and used as the reference standard for lesion segmentation and lesion-guided model training.

All CT images were preprocessed using a standardized pipeline. Voxel spacing was resampled to $1.0 \times 1.0 \times 1.0$ mm³ using trilinear interpolation. Hounsfield unit (HU) values

were clipped to the range [−1000, 400] to retain lung parenchyma and soft-tissue information, followed by min-max normalization to [0, 1]. For each patient, a single dominant target nodule was selected for analysis; in patients with multiple nodules, the nodule with the largest diameter was chosen. A cubic patch of 64×64×64 voxels centered on the lesion centroid was extracted as model input. Lesion masks were resampled to match the spatial dimensions of the deepest encoder feature map for feature interaction.

2.2 Study Methods

2.2.1. Model Design: Lesion-Guided Dual-Branch UNet (LG-DU-Net)

To improve lesion representation and enable joint optimization of segmentation and classification, we developed a **Lesion-Guided Dual-Branch UNet (LG-DU-Net)**, an end-to-end 3D deep learning framework based on the conventional UNet architecture. The network consists of four components: (1) an encoder–decoder segmentation module, (2) a lesion feature enhancement branch, (3) an adaptive classification branch, and (4) a cross-task collaborative optimization module (Figure 2).

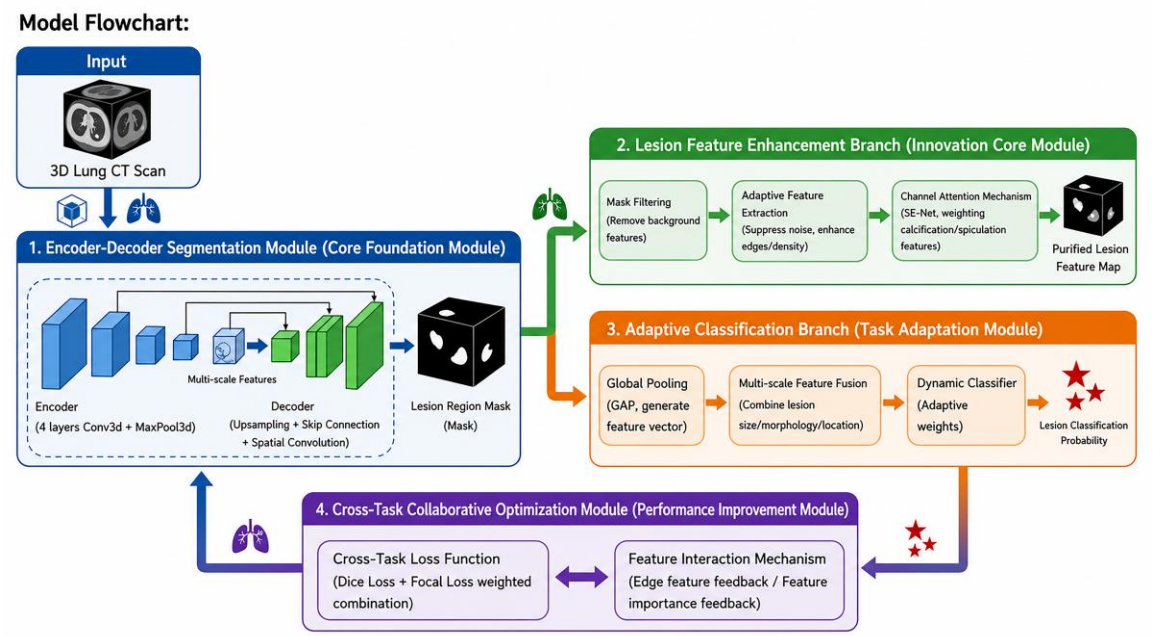


Figure 2 Model Flowchart

a) Encoder–decoder segmentation module.

The segmentation branch adopts a conventional 3D-UNet encoder–decoder architecture with four convolutional blocks and skip connections. Dilated convolutions were incorporated to enlarge the receptive field while preserving spatial resolution. The decoder generates a voxel-level lesion mask that provides spatial guidance for subsequent feature extraction and classification.

b) Lesion feature enhancement branch.

The predicted lesion mask was applied to the deepest encoder feature map to suppress irrelevant background information and preserve lesion-specific features. A 1×1×1 convolution followed by a sigmoid activation was used for feature refinement, and a squeeze-and-excitation (SE) attention module further recalibrated channel-wise feature responses to enhance discriminative lesion representations.

c) Adaptive classification branch.

The refined lesion features were subjected to global average pooling and fused with multi-scale encoder features to generate a comprehensive lesion representation. The fused features were subsequently processed by a classification head to predict lesion categories.

d) Cross-task collaborative optimization.

Segmentation and classification were jointly optimized using a hybrid loss function consisting of Dice loss and Focal loss. In addition, feature interaction between the segmentation and classification branches enabled shared optimization, allowing lesion localization and classification to mutually reinforce each other during network training.

The network employs three-dimensional convolutions throughout to preserve volumetric information and capture inter-slice contextual features of pulmonary nodules, thereby providing a more comprehensive representation of lesion morphology than conventional two-dimensional convolutions.

2.2.2. Data Distribution

A total of **1,084** patients CT scans were included in this study. The dataset was randomly divided into training (80%) and test (20%) sets at the patient level. The distribution of each disease category is summarized in Table 1.

Table 1. Data distribution of the training and test sets

Category	Total	Training set (80%)	Test set (20%)
Pulmonary cryptococcosis	298	238	60
Tuberculosis	240	192	48
Granulomatous inflammation	252	202	50

Lung malignancy	294	235	59
Total	1084	867	217

2.2.3. Model Training and Evaluation

All models were trained using the same training strategy to ensure a fair comparison. Five-fold cross-validation was performed on the training set for model development and hyperparameter optimization, while the independent test set was reserved for final performance evaluation.

Model training was performed using the AdamW optimizer with an initial learning rate of 1×10^{-4}, cosine annealing learning rate scheduling, and a weight decay of 1×10^{-4}. The batch size was set to 8, and the maximum number of training epochs was 200. Early stopping was applied when the validation loss did not improve for 20 consecutive epochs. Data augmentation included random rotation (±15°), horizontal and vertical flipping, random scaling (0.8–1.2), and random noise addition.

The network was jointly optimized using a weighted combination of Dice loss and Focal loss, with weights of 0.4 and 0.6, respectively. Dice loss was used to optimize lesion segmentation, whereas Focal loss addressed class imbalance in the classification task. The focusing parameter γ was set to 2.0, and the class-balancing parameter α was dynamically adjusted according to the class distribution.

Model performance was evaluated using the area under the receiver operating characteristic curve (AUC), accuracy, sensitivity, specificity, positive predictive value (PPV), negative predictive value (NPV), and *F*1 score. For the three-class classification

task, macro-averaged AUC and *F*1 score were additionally calculated. Differences in AUC between models were assessed using the DeLong test, with $P < 0.05$ considered statistically significant. Statistical analyses were performed using Python 3.10 with the scikit-learn and SciPy libraries.

2.2.4. Baseline Models

To evaluate the performance of the proposed LG-DU-Net, five representative deep learning models were selected as baseline methods for comparison: 2D-ResNet50**,** 2D-EfficientNet-B4**,** 3D-ResNet18**,** 3D-DenseNet121**,** and 3D-SE-ResNeXt-50**.** These models represent widely used convolutional neural network architectures for medical image classification and volumetric image analysis. For a fair comparison, all baseline models were trained using the same training and test datasets, with identical data preprocessing, data augmentation, optimization strategy, and evaluation metrics as those used for LG-DU-Net.

3.Results

3.1 General Characteristics of Demographic Data

Among the 240 patients with pulmonary tuberculous nodules, 176 were male (73.3%) and 64 were female (26.7%), with an average age of 56.9 ± 12.1 years. Eighteen patients (7.5%) had a clear history of previous tuberculosis. Eighty-seven patients (36.2%) had potentially immunocompromising comorbidities, including 17 cases of malignant tumors, 73 cases of diabetes, and 3 patients with more than one disease. In terms of clinical

manifestations, the vast majority of patients had no typical symptoms, especially lacking respiratory symptoms such as cough and expectoration (Table 2).

Table 2. Clinical characteristics and preoperative examination results of 240 patients with tuberculous pulmonary nodules

Variable	n (%) or Mean±SD	Variable	n (%)
Age	56.9±12.1	**Underlying Condition**	
<25	0 (0.0)	Chronic Lung Disease	23 (9.6)
25-44	38 (15.8)	Malignancy	17 (7.1)
45-59	92 (38.3)	Hypertension	62 (25.8)
60-74	101 (42.1)	Diabetes Mellitus	73 (30.4)
≥75	9 (3.8)	Cardiovascular Disease	23 (9.6)
Sex		**Tumor Marker**	
Male	176 (73.3)	CA125	7 (2.9)
Female	64 (26.7)	Ferritin	44 (18.3)
Career		CEA	25 (10.4)
Services	7 (2.9)	CK19	11 (4.6)
Business	36 (15.0)	SCC-Ag	9 (3.8)
Farmer	16 (6.7)	**Systemic Symptom**	
Labor	89 (37.1)	Fatigue	7 (2.9)
Other	92 (38.3)	Fever	7 (2.9)
History of TB	18 (7.5)	Cough	0
Preoperative Tests		phlegm	0
Pathogenic Examination	41(17.1)	Night Sweat	0
Sputum Culture	19(7.9)	Nodule Position	
Negative	19	Right Middle Lobe	83(34.6)
Sputum Smear	22(9.2)	Left Lower Lobe	63(26.3)
Negative	22	**Postoperative Treatment**	
GeneXpert	13(5.4)	Under anti-TB therapy	152 (63.3)
Negative	13	No anti-TB therapy	75（31.3)
TSPOT	39(16.3)	Lost Connection	13（5.4）

Positive	29
Negative	10

Only 39 patients with pulmonary tuberculous nodules underwent T-SPOT testing preoperatively, of which 29 (74.4%) were positive; 13 patients underwent sputum GeneXpert testing preoperatively, none of them were positive; no positive results were found in patients who underwent preoperative sputum Mycobacterium tuberculosis culture and sputum Mycobacterium tuberculosis smear.

3.2 Model Performance

a) Benign–Malignant Classification

The test set included **158 benign** and **59 malignant** pulmonary nodules. As shown in **Figure 3**, LG-DU-Net achieved the best performance among all evaluated models, with an **AUC of 0.880**, **accuracy of 84.7%**, **sensitivity of 85.2%**, and **specificity of 84.5%**. The AUC was significantly higher than those of **2D-ResNet50 (0.775)**, **2D-EfficientNet-B4 (0.798)**, **3D-ResNet18 (0.806)**, **3D-DenseNet121 (0.821)**, and **3D-SE-ResNeXt-50 (0.841)** (DeLong test, $P < 0.05$) as showed in Table3. The detailed performance metrics are provided in **Supplementary Table S1**.

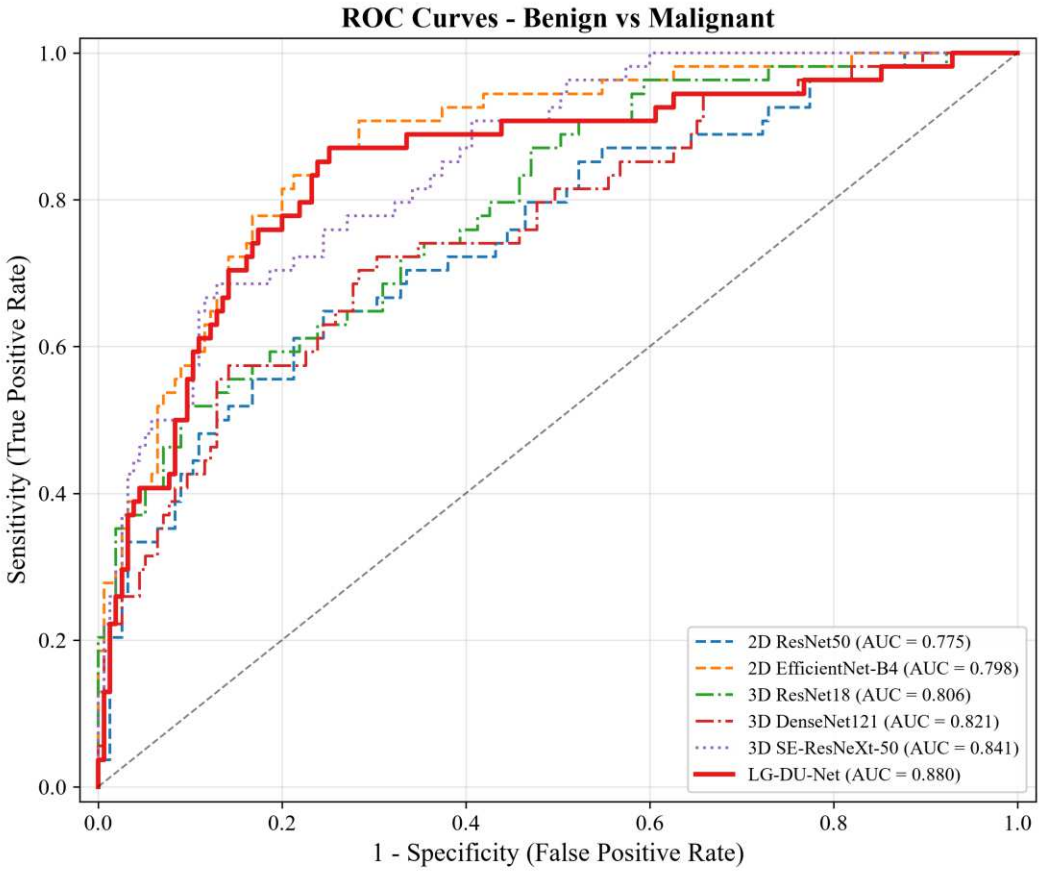


Figure 3. ROC curves of different models for benign versus malignant classification

Table 3. AUC comparison of different models across classification tasks

Task	2D-ResNet50	2D-EfficientNet-B4	3D-ResNet18	3D-DenseNet121	3D-SE-ResNeXt-50	LG-DU-Net
Benign vs. Malignant	0.775	0.798	0.806	0.821	0.841	0.880
TB vs. Cancer	0.768	0.789	0.798	0.812	0.833	0.872
TB vs. Granuloma	0.751	0.773	0.782	0.796	0.818	0.855
TB vs Cryptococcosis	0.861	0.879	0.903	0.928	0.951	0.972
TB vs. Granuloma vs. Crypto (3-class, macro-AUC)	0.735	0.758	0.772	0.791	0.825	0.862

Note: The AUC of LG-DU-Net in all tasks was significantly superior to that of the baseline models (DeLong test, $P<0.05$). The macro-average AUC was reported for the three-class classification task. Detailed performance metrics are provided in Supplementary Tables S1-S5.

b) Pulmonary Tuberculosis versus Lung Cancer

The test set comprised **48** patients with pulmonary tuberculosis and **54** with lung cancer. As shown in **Figure 4**, LG-DU-Net achieved an **AUC of 0.872**, **accuracy of 85.3%**, **sensitivity of 90.7%**, and **specificity of 79.2%**, significantly outperforming all baseline models (all $P < 0.05$). The detailed performance metrics are presented in **Supplementary Table S2**.

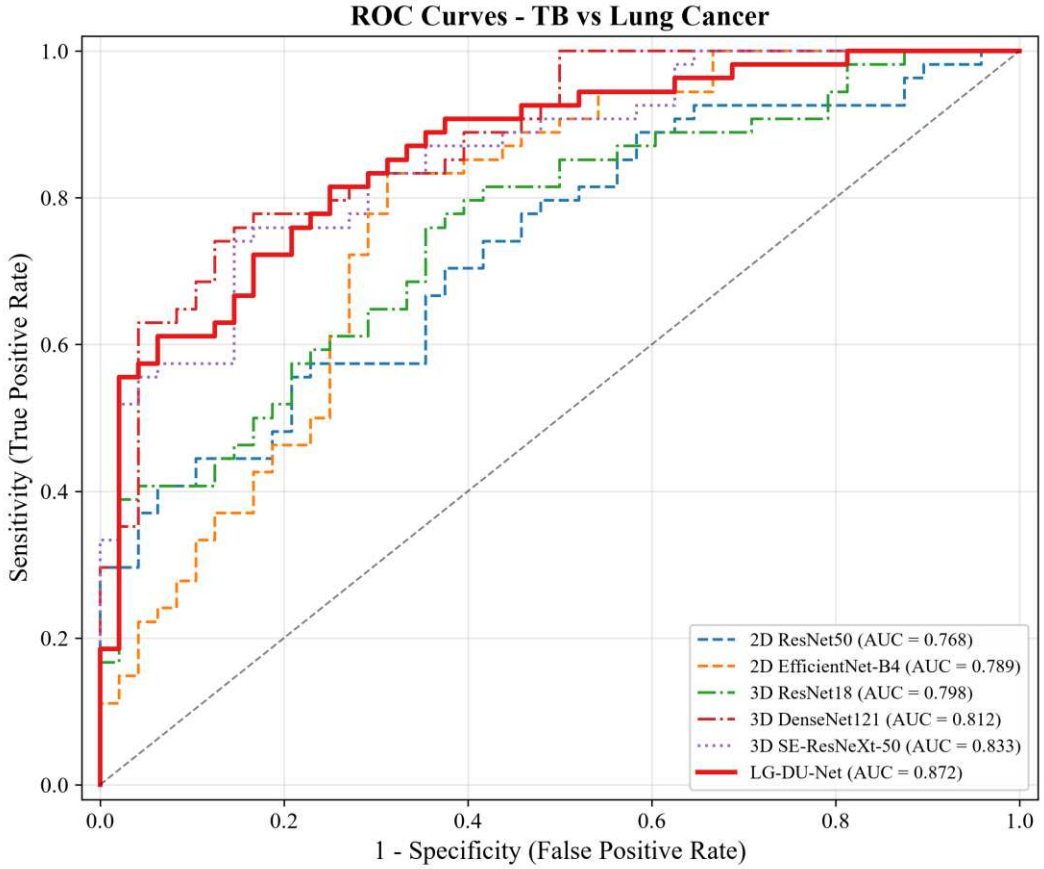


Figure 4. ROC curves of different models for tuberculosis versus lung cancer classification

c) Pulmonary Tuberculosis versus Other Granulomatous Inflammatory Lesions

The test set included **48** patients with pulmonary tuberculosis and **50** with other granulomatous inflammatory lesions. As shown in **Figure 5**, LG-DU-Net achieved an **AUC of 0.855**, **accuracy of 77.6%**, **sensitivity of 80.0%**, and **specificity of 75.0%**. The AUC of LG-DU-Net was significantly higher than those of all baseline models (all $P < 0.05$). The detailed performance metrics are provided in **Supplementary Table S3**.

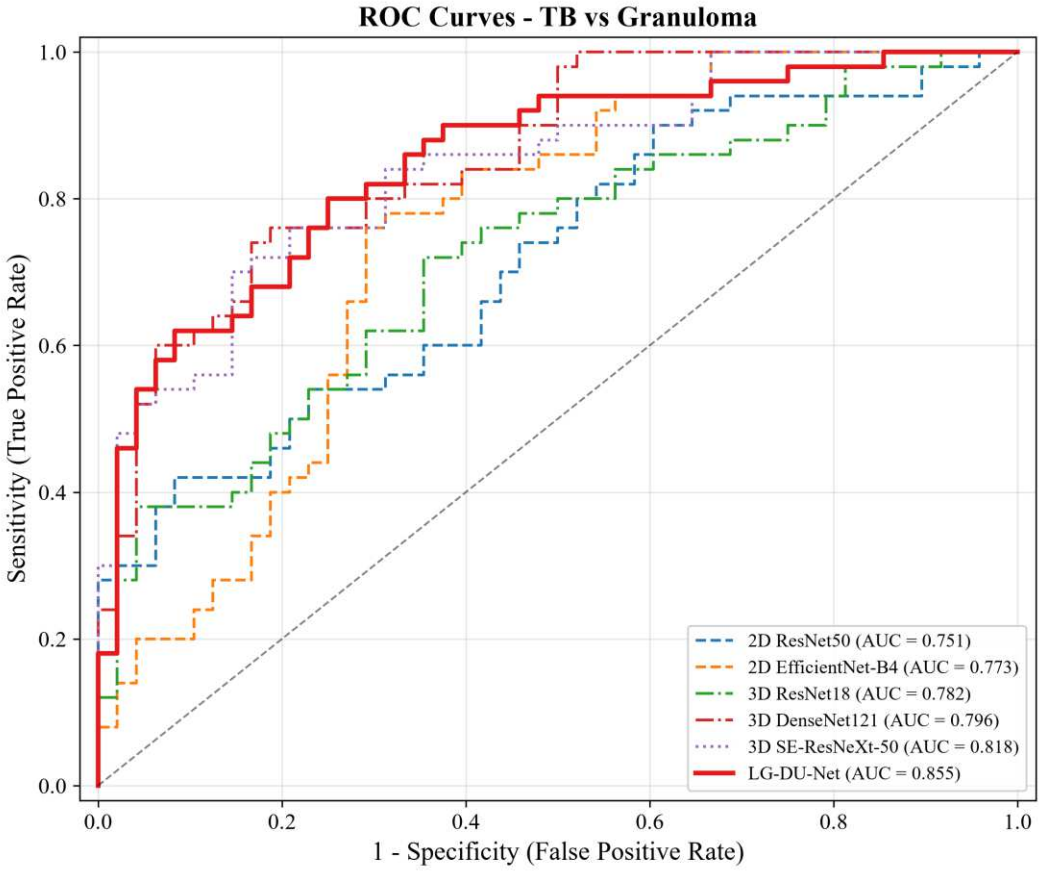


Figure 5. ROC curves of different models for tuberculosis versus granuloma classification

d) Pulmonary Tuberculosis versus Pulmonary Cryptococcosis

The test set comprised **48** patients with pulmonary tuberculosis and **60** with pulmonary cryptococcosis. As shown in **Figure 6**, LG-DU-Net achieved the highest AUC among all

binary classification tasks, with an **AUC of 0.972**, **accuracy of 89.8%**, **sensitivity of 91.7%**, and **specificity of 87.5%**, and its AUC was also the highest one among all baseline models (all $P < 0.05$). The detailed performance metrics are summarized in **Supplementary Table S4**.

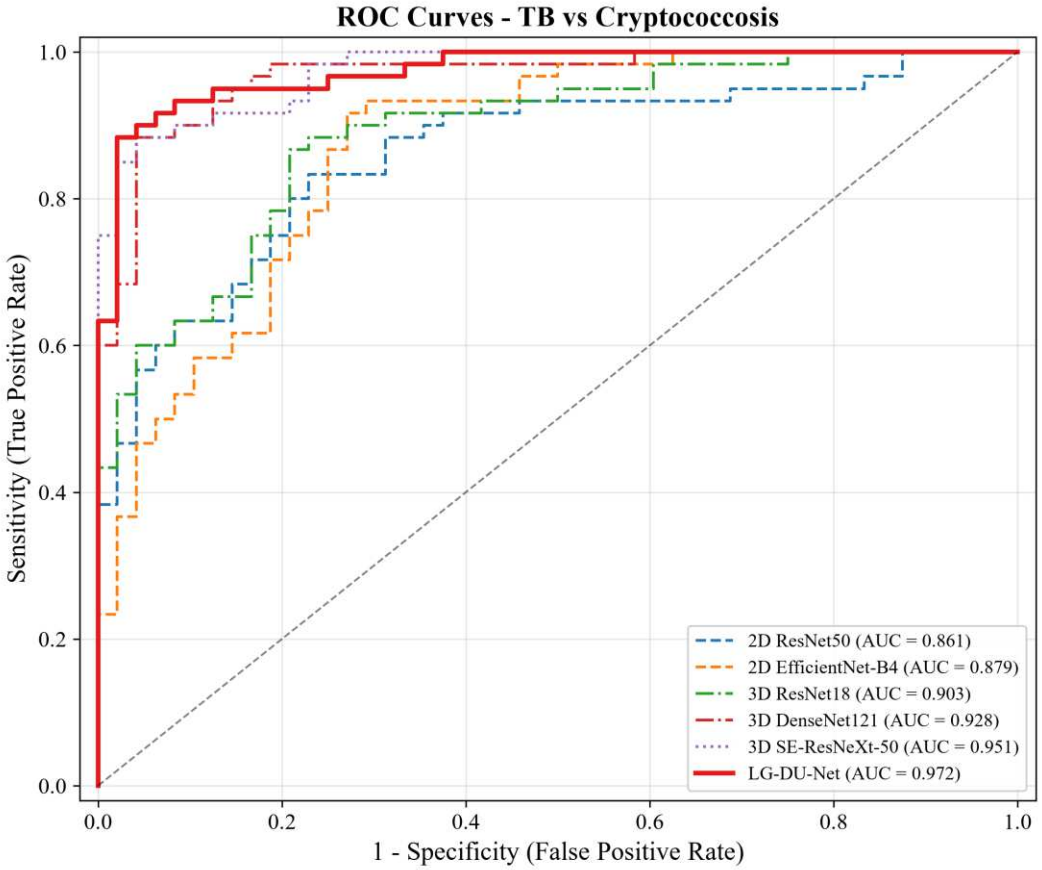


Figure 6. ROC curves of different models for tuberculosis versus pulmonary cryptococcosis classification

e) Three-Class Classification

The three-class classification task included **48** patients with pulmonary tuberculosis, **50** with other granulomatous inflammatory lesions, and **60** with pulmonary cryptococcosis.

As shown in **Figure 7**, LG-DU-Net achieved an **overall accuracy of 74.7%**, a **macro-average AUC of 0.862**, and a **macro-average *F*1 score of 0.739**. Among the three disease categories, pulmonary cryptococcosis achieved the highest one-versus-rest AUC (**0.935**), followed by pulmonary tuberculosis (**0.845**) and granulomatous inflammatory lesions (**0.806**). The macro-average AUC of LG-DU-Net was significantly higher than those of all baseline models (all $P < 0.05$). Detailed performance metrics are provided in **Supplementary Table S5**.

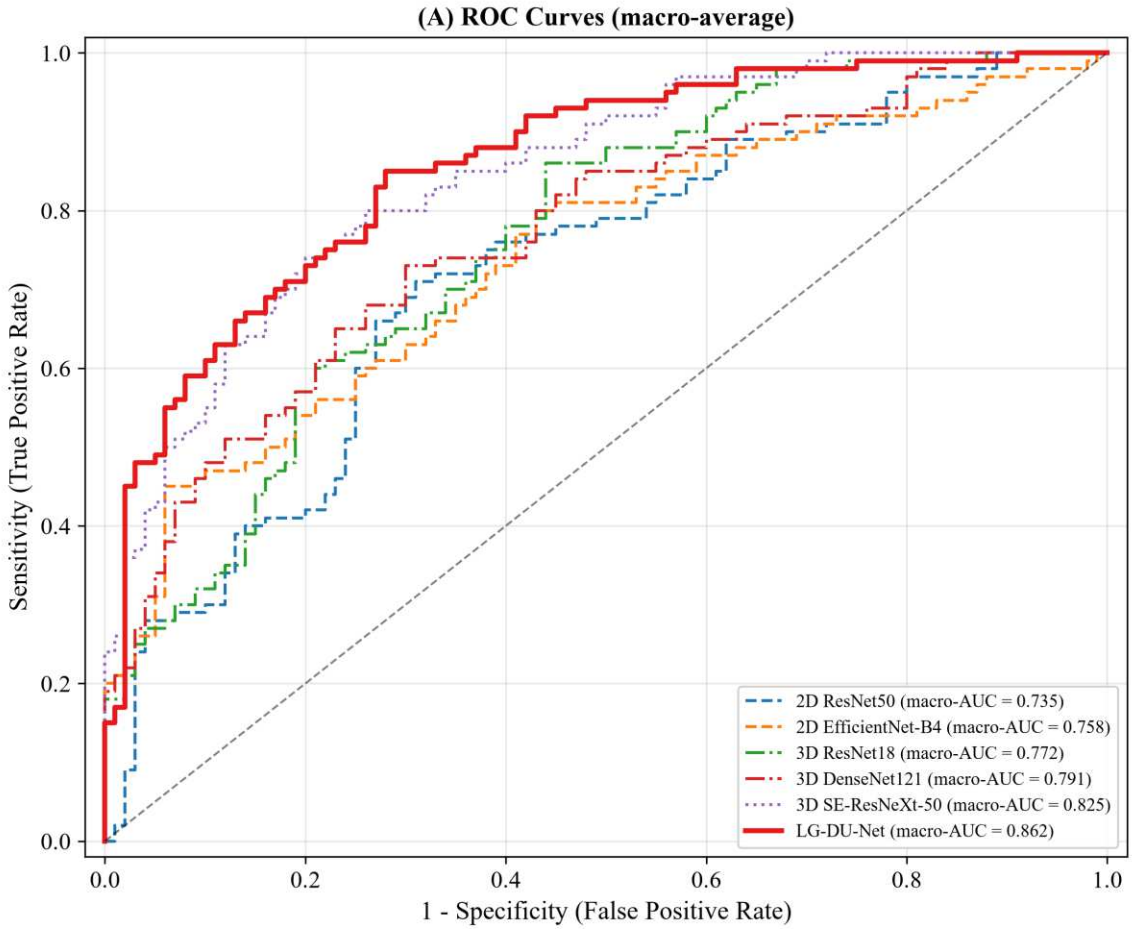


Figure 7. Three-class classification of tuberculosis, granuloma, and pulmonary cryptococcosis. ROC curves of different models (macro-average)

3.3 Grad-CAM Interpretability Analysis

To investigate the decision-making process of LG-DU-Net, Gradient-weighted Class Activation Mapping (Grad-CAM) was used to visualize the regions contributing to model predictions (**Figure 8**). In the benign–malignant classification task, the model primarily focused on the nodule margins and adjacent lung parenchyma for benign nodules, whereas attention for malignant nodules was concentrated on regions of heterogeneous internal density and spiculated margins. In the three-class classification task, Grad-CAM highlighted calcification and satellite lesions for pulmonary tuberculosis, perinodular ground-glass opacity for granulomatous inflammatory lesions, and the halo sign for pulmonary cryptococcosis. The Grad-CAM visualizations demonstrated that LG-DU-Net consistently focused on lesion-related imaging features rather than surrounding background regions.

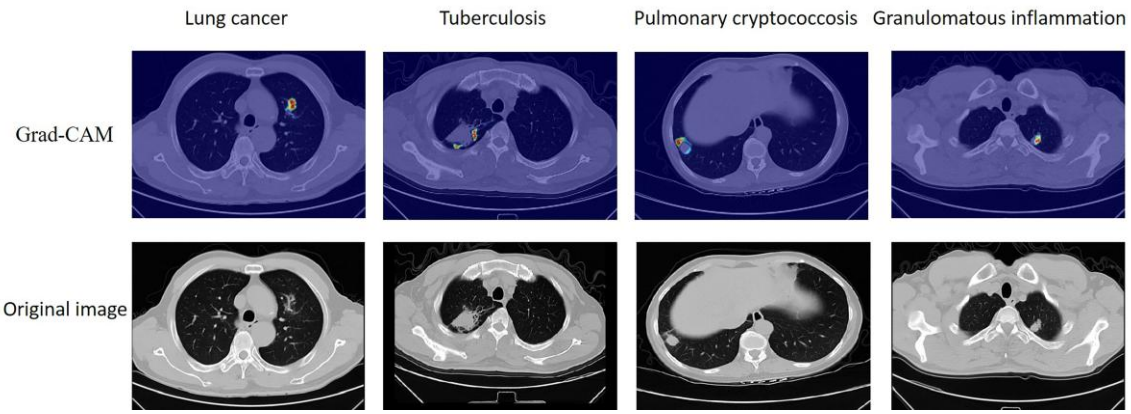


Figure 8. Grad-CAM visualization of LG-DU-Net across different classification tasks. For each case, the left half shows the original CT image and the right half shows the Grad-CAM heatmap overlay. Red regions indicate areas with high attention weights. (a) Malignant nodule: attention on internal density heterogeneity and spiculation; (b) Tuberculosis: attention on calcification and satellite lesions; (c) Pulmonary cryptococcosis: attention on halo sign; (d) Granulomatous inflammation: attention on perinodular ground-glass opacity;

4. Discussion

In this study, we developed a lesion-guided deep learning framework (LG-DU-Net) for the differential diagnosis of pulmonary nodules using chest CT images. Based on a surgically confirmed cohort of 1,084 patients, the proposed framework consistently outperformed five representative deep learning models across benign–malignant classification, multiple binary classification tasks, and three-class classification of infectious pulmonary nodules. Notably, LG-DU-Net achieved its highest diagnostic performance in differentiating pulmonary tuberculosis from pulmonary cryptococcosis. Grad-CAM visualization further demonstrated that the model primarily focused on lesion-related imaging features rather than surrounding normal lung parenchyma, supporting the interpretability of the proposed framework.

The favorable performance of LG-DU-Net is likely attributable to its lesion-guided design and end-to-end optimization strategy. Conventional deep learning models typically analyze the entire CT volume, in which pulmonary nodules occupy only a small proportion of the image, allowing irrelevant background structures to interfere with feature extraction. In contrast, the lesion-guided mechanism directs the network toward lesion-specific imaging characteristics while suppressing background information[17, 21]. Furthermore, segmentation and classification are jointly optimized within a unified framework, allowing lesion localization and disease recognition to reinforce each other during training[22-24]. The incorporation of three-dimensional convolutions further enables preservation of volumetric contextual information and improves characterization

of complex lesion morphology, which is particularly important for differentiating infectious pulmonary nodules with subtle imaging differences[21, 25].

From a clinical perspective, accurate preoperative differentiation of pulmonary nodules remains challenging because pulmonary tuberculosis, pulmonary cryptococcosis, and other granulomatous inflammatory lesions frequently mimic lung cancer on CT. These diseases often share overlapping imaging features, including lobulation, spiculation, cavitation, calcification, and satellite lesions, making visual interpretation difficult even for experienced radiologists. Incorrect diagnosis may result in unnecessary surgical resection or delayed initiation of appropriate antimicrobial therapy. In the present study, LG-DU-Net achieved the highest performance in differentiating pulmonary tuberculosis from pulmonary cryptococcosis. Although these diseases share many radiological characteristics, pulmonary tuberculosis is more frequently associated with satellite lesions, bronchogenic dissemination, focal fibrosis, and coarse calcification, whereas pulmonary cryptococcosis more commonly presents with smooth margins, halo signs, and relatively homogeneous internal attenuation. These subtle differences are difficult to quantify using conventional visual assessment but can be effectively captured through hierarchical deep feature learning.

Compared with previous studies, our work provides several methodological and clinical advantages. Most existing artificial intelligence studies have focused on differentiating pulmonary tuberculosis from lung cancer or distinguishing benign from malignant pulmonary nodules using radiomics or conventional convolutional neural networks[2, 4, 20, 26]. Many of these approaches rely on manual lesion delineation, which is labor-

intensive and susceptible to interobserver variability. Moreover, previous studies have predominantly evaluated binary classification tasks and have rarely included pulmonary cryptococcosis or other granulomatous inflammatory lesions. In contrast, LG-DU-Net performs end-to-end lesion segmentation and classification without manual feature engineering and evaluates multiple clinically relevant diagnostic scenarios within a single framework. More importantly, all diagnostic labels in this study were established by postoperative histopathology, providing a reliable reference standard for model development and evaluation. The inclusion of four clinically important pathological categories better reflects the spectrum of pulmonary nodules encountered in routine clinical practice and therefore enhances the potential translational value of the proposed framework.

Beyond improving diagnostic accuracy, the proposed framework may also influence clinical decision-making. In tuberculosis-endemic regions, pulmonary tuberculous nodules are frequently mistaken for malignant tumors because of their nonspecific CT manifestations. An accurate and interpretable deep learning model may therefore provide objective decision support before invasive procedures. For patients predicted to have pulmonary tuberculosis or other benign infectious lesions, the model may provide additional decision support when selecting patients for further diagnostic evaluation, such as bronchoscopy, nucleic acid amplification testing, mycobacterial culture, or short-term imaging follow-up, thereby reducing unnecessary surgical intervention while facilitating timely diagnosis and appropriate treatment. In addition, the fully automated workflow makes the proposed framework potentially valuable for primary hospitals where experienced thoracic radiologists are not readily available. A major strength of this study

is the use of a relatively large surgically confirmed cohort covering four clinically important pathological categories, providing a reliable reference standard for model development and evaluation.

Several limitations should be acknowledged. First, this was a retrospective single-center study, and external multicenter validation is required before routine clinical application. Second, all pulmonary tuberculosis cases were surgically resected and pathologically confirmed, introducing potential selection bias toward atypical lesions requiring surgery. Consequently, the model has not yet been validated in patients with clinically diagnosed pulmonary tuberculosis who did not undergo surgical intervention. Third, the proposed framework relied exclusively on CT images without incorporating clinical information, laboratory findings, or microbiological results. Future multimodal models integrating imaging with clinical data may further improve diagnostic performance and clinical applicability. Finally, although LG-DU-Net consistently outperformed all baseline models, differentiation between pulmonary tuberculosis and other granulomatous inflammatory lesions remains relatively challenging, suggesting that larger multicenter datasets and further optimization of model architecture are warranted.

5. Conclusion

We developed a lesion-guided deep learning framework for the differential diagnosis of pulmonary nodules using chest CT. Using a large surgically confirmed cohort, LG-DU-Net consistently outperformed representative two-dimensional and three-dimensional deep learning models across multiple clinically relevant diagnostic tasks. The proposed framework demonstrated particularly strong performance in differentiating pulmonary

tuberculosis from pulmonary cryptococcosis, highlighting its potential to improve preoperative diagnosis, facilitate appropriate clinical management, and reduce unnecessary surgical intervention. Prospective multicenter validation will be essential before routine clinical implementation.

Conflict of Interests

The authors declare that they have no conflicts of interest.

Funding Declaration

This study was supported by the Prevention and Control of Emerging and Major Infectious Diseases-National Science and Technology Major Project （2025ZD01908700）;National Key Research and Development Program of China, grant No.2020YFE0204300

References

1. Beig N, Khorrami M, Alilou M, Prasanna P, Braman N, Orooji M, Rakshit S, Bera K, Rajiah P, Ginsberg J *et al*: **Perinodular and Intranodular Radiomic Features on Lung CT Images Distinguish Adenocarcinomas from Granulomas**. *Radiology* 2019, **290**(3):783-792.
2. Zhao W, Xiong Z, Jiang Y, Wang K, Zhao M, Lu X, Liu A, Qin D, Li Z: **Radiomics based on enhanced CT for differentiating between pulmonary tuberculosis and pulmonary adenocarcinoma presenting as solid nodules or masses**. *J Cancer Res Clin Oncol* 2023, **149**(7):3395-3408.
3. Lim JU: **Impact of pulmonary tuberculosis on lung cancer screening: a narrative review**. *Ewha Med J* 2025, **48**(2):e23.
4. Cui EN, Yu T, Shang SJ, Wang XY, Jin YL, Dong Y, Zhao H, Luo YH, Jiang XR: **Radiomics model for distinguishing tuberculosis and lung cancer on computed tomography scans**. *World J Clin Cases* 2020, **8**(21):5203-5212.
5. Ge YL, Liu CH, Wang MH, Li ZZ, Li HL, Cui ZY, Zhang HF, Zhu XY, Zhang X, Yu HL *et al*: **Serum Cryptococcal Antigen Confirmed Pulmonary Cryptococcosis in an Immune-competent Adult Firstly Misdiagnosed of Tuberculosis from a Lung Biopsy: a Case Report and Literature Review**. *Clin Lab* 2018, **64**(11).
6. Wang D, Wu C, Gao J, Zhao S, Ma X, Wei B, Feng L, Wang Y, Xue X: **Comparative study of primary pulmonary cryptococcosis with multiple nodules or masses by CT and pathology**. *Exp Ther Med* 2018, **16**(6):4437-4444.
7. Xia Z, Qiao K, He J: **Recent advances in the management of pulmonary tuberculoma with focus on the use of tubeless video-assisted thoracoscopic surgery**. *J Thorac Dis* 2017, **9**(9):3307-3312.
8. Wang Z, Xin J, Sun P, Lin Z, Yao Y, Gao X: **Improved lung nodule diagnosis accuracy using lung CT images with uncertain class**. *Comput Methods Programs Biomed* 2018, **162**:197-209.
9. Causey JL, Zhang J, Ma S, Jiang B, Qualls JA, Politte DG, Prior F, Zhang S, Huang X: **Highly accurate model for prediction of lung nodule malignancy with CT scans**. *Sci Rep* 2018, **8**(1):9286.
10. Nijiati M, Zhou R, Damaola M, Hu C, Li L, Qian B, Abulizi A, Kaisaier A, Cai C, Li H *et al*: **Deep learning based CT images automatic analysis model for active/non-active pulmonary tuberculosis differential diagnosis**. *Front Mol Biosci* 2022, **9**:1086047.
11. Khorrami M, Bera K, Thawani R, Rajiah P, Gupta A, Fu P, Linden P, Pennell N, Jacono F, Gilkeson RC *et al*: **Distinguishing granulomas from adenocarcinomas by integrating stable and discriminating radiomic features on non-contrast computed tomography scans**. *Eur J Cancer* 2021, **148**:146-158.
12. Hogeweg L, Sanchez CI, Maduskar P, Philipsen R, Story A, Dawson R, Theron G, Dheda K, Peters-Bax L, van Ginneken B: **Automatic Detection of Tuberculosis in Chest Radiographs Using a Combination of Textural, Focal, and Shape Abnormality Analysis**. *IEEE Trans Med Imaging* 2015, **34**(12):2429-2442.
13. Park S, Lee SM, Kim W, Park H, Jung KH, Do KH, Seo JB: **Computer-aided Detection of Subsolid Nodules at Chest CT: Improved Performance with Deep Learning-based CT Section Thickness Reduction**. *Radiology* 2021, **299**(1):211-219.
14. Owais M, Arsalan M, Mahmood T, Kim YH, Park KR: **Comprehensive Computer-Aided Decision Support Framework to Diagnose Tuberculosis From Chest X-Ray Images: Data Mining Study**. *JMIR Med Inform* 2020, **8**(12):e21790.
15. Choe J, Lee SM, Do KH, Lee G, Lee JG, Lee SM, Seo JB: **Deep Learning-based Image Conversion of CT Reconstruction Kernels Improves Radiomics Reproducibility for Pulmonary Nodules or Masses**. *Radiology* 2019, **292**(2):365-373.
16. Gao C, Wu L, Wu W, Huang Y, Wang X, Sun Z, Xu M, Gao C: **Deep learning in pulmonary nodule detection and segmentation: a systematic review**. *Eur Radiol* 2025, **35**(1):255-266.
17. Lakhani P, Sundaram B: **Deep Learning at Chest Radiography: Automated Classification of Pulmonary Tuberculosis by Using Convolutional Neural Networks**. *Radiology* 2017, **284**(2):574-582.
18. Wu G, Woodruff HC, Shen J, Refaee T, Sanduleanu S, Ibrahim A, Leijenaar RTH, Wang R, Xiong J, Bian J *et al*: **Diagnosis of Invasive Lung Adenocarcinoma Based on Chest CT**

Radiomic Features of Part-Solid Pulmonary Nodules: A Multicenter Study. *Radiology* 2020, **297**(2):451-458.

19. Li Y, Lyu B, Wang R, Peng Y, Ran H, Zhou B, Liu Y, Bai G, Huai Q, Chen X *et al*: **Machine learning-based radiomics to distinguish pulmonary nodules between lung adenocarcinoma and tuberculosis**. *Thorac Cancer* 2024, **15**(6):466-476.
20. Feng B, Chen X, Chen Y, Liu K, Li K, Liu X, Yao N, Li Z, Li R, Zhang C *et al*: **Radiomics nomogram for preoperative differentiation of lung tuberculoma from adenocarcinoma in solitary pulmonary solid nodule**. *Eur J Radiol* 2020, **128**:109022.
21. Ardila D, Kiraly AP, Bharadwaj S, Choi B, Reicher JJ, Peng L, Tse D, Etemadi M, Ye W, Corrado G *et al*: **End-to-end lung cancer screening with three-dimensional deep learning on low-dose chest computed tomography**. *Nat Med* 2019, **25**(6):954-961.
22. Tang T, Zhang R: **A Multi-Task Model for Pulmonary Nodule Segmentation and Classification**. *J Imaging* 2024, **10**(9).
23. Wang Y, Zhou C, Chan HP, Hadjiiski LM, Chughtai A, Kazerooni EA: **Hybrid U-Net-based deep learning model for volume segmentation of lung nodules in CT images**. *Med Phys* 2022, **49**(11):7287-7302.
24. Wang M, An X, Pei Z, Li N, Zhang L, Liu G, Ming D: **An Efficient Multi-Task Synergetic Network for Polyp Segmentation and Classification**. *IEEE J Biomed Health Inform* 2024, **28**(3):1228-1239.
25. Gong L, Jiang S, Yang Z, Zhang G, Wang L: **Automated pulmonary nodule detection in CT images using 3D deep squeeze-and-excitation networks**. *Int J Comput Assist Radiol Surg* 2019, **14**(11):1969-1979.
26. Lambin P, Rios-Velazquez E, Leijenaar R, Carvalho S, van Stiphout RG, Granton P, Zegers CM, Gillies R, Boellard R, Dekker A *et al*: **Radiomics: extracting more information from medical images using advanced feature analysis**. *Eur J Cancer* 2012, **48**(4):441-446.

Supplementary Files

This is a list of supplementary files associated with this preprint. Click to download.

- supplementarytable.docx